UC San Diego
UC San Diego Previously Published Works

Title

A Conserved Ectodomain-Transmembrane Domain Linker Motif Tunes the Allosteric Regulation of Cell Surface Receptors*

Permalink

https://escholarship.org/uc/item/6bk3t6t8

Journal

Journal of Biological Chemistry, 291(34)

ISSN

0021-9258

Authors

Schmidt, Thomas

Ye, Feng

Situ, Alan J

et al.

Publication Date

2016-08-01

DOI

10.1074/jbc.m116.733683

A Conserved Ectodomain-Transmembrane Domain Linker Motif Tunes the Allosteric Regulation of Cell Surface Receptors*�S

Thomas Schmidt[‡1], **Feng Ye**[§], **Alan J. Situ**[‡], **Woojin An**[¶], **Mark H. Ginsberg**[§], and **Tobias S. Ulmer**[‡2]

From the ‡Department of Biochemistry & Molecular Biology and Zilkha Neurogenetic Institute, Keck School of Medicine, University of Southern California, Los Angeles, California 90033, the §Department of Medicine, University of California San Diego, La Jolla, California 92093, and the ¶Department of Biochemistry & Molecular Biology and Norris Comprehensive Cancer Center, University of Southern California, Los Angeles, California 90033

In many families of cell surface receptors, a single transmembrane (TM) α-helix separates ecto- and cytosolic domains. A defined coupling of ecto- and TM domains must be essential to allosteric receptor regulation but remains little understood. Here, we characterize the linker structure, dynamics, and resulting ecto-TM domain coupling of integrin αIIb in model constructs and relate it to other integrin α subunits by mutagenesis. Cellular integrin activation assays subsequently validate the findings in intact receptors. Our results indicate a flexible yet carefully tuned ecto-TM coupling that modulates the signaling threshold of integrin receptors. Interestingly, a proline at the N-terminal TM helix border, termed NBP, is critical to linker flexibility in integrins. NBP is further predicted in 21% of human single-pass TM proteins and validated in cytokine receptors by the TM domain structure of the cytokine receptor common subunit β and its P441A-substituted variant. Thus, NBP is a conserved uncoupling motif of the ecto-TM domain transition and the degree of ecto-TM domain coupling represents an important parameter in the allosteric regulation of diverse cell surface receptors.

Cells sense their environment through transmembrane (TM)[3] surface receptors that transmit extracellular signals into the cell. With the exception of G-protein coupled receptors, these proteins are dimers composed of subunits that each typically exhibits an extracellular domain (ectodomain) containing the ligand-binding site, a single TM α-helix, and an intracellular effector domain. Integrins, which control vital cell-cell and cell-matrix adhesions (1–3), constitute one ubiquitous family of TM cell surface receptors. Receptor-tyrosine kinases represent another prominent family that activate upon the stabilization of dimeric receptor states by bound ligand (4, 5). However, rather than being simple binary switches, all these receptors have the potential for allosteric regulation (1, 5, 6), indicating a multi-state coupling of ecto- and TM domains. This coupling and associated allosteric parameters must depend on the structural and dynamic properties of the linker between ecto- and TM domains. However, irrespective of detailed structural information on ecto- and TM domain in receptor-tyrosine kinases (4, 5), structural or dynamic information on linkers remains indirect and ambiguous (7–9). Similarly, structures of integrin ectodomains, TM domains, and cytosolic tails are available (10–16) but little is known about their ecto-TM domain coupling. In support of a functionally relevant linker, integrin αMβ2 spontaneously activates when the TM domain is uncoupled from the ectodomain by insertion of a flexible (GGGGS)$_2$ linker (17).

Integrins consist of heterodimeric, non-covalently associated αβ subunits that each exhibits a large ectodomain, a single TM α-helix, and a short cytosolic tail (Fig. 1A). In addition to outside-in signaling, integrins also signal in the opposite direction (inside-out signaling) in relationship to their function as dynamic cell adhesion molecules (1–3). This bidirectional, multistate signaling ability renders integrins well suited to study the structural basis of ecto-TM coupling and its impact on allosteric receptor regulation. The framework of allosteric integrin regulation is established by a coupling between the structural state of αβ ectodomains and the association state of αβ TM domains (12, 18). The assembled TM complex correlates with the low affinity, bent conformation of the ectodomains and the absence of signaling (Fig. 1A). During inside-out signaling, binding of an agonist to the cytosolic β tail disrupts the TM complex (19), thereupon destabilizing the interface of subdomains α(Calf2)-β(I-EGF4/β-tail) within the ectodomains (20, 21), and permitting ligand binding by the rearranged, high affinity ectodomains (Fig. 1A). When an extracellular agonist is able to spontaneously bind the ectodomains and dissociate the α(Calf2)-β(I-EGF4/β-tail) interface, the destabilized TM complex can dissociate giving rise to outside-in signaling (21, 22).

[1] Present address: Laboratory of Chemical Physics, NIDDK, National Institutes of Health, Bethesda, MD 20892.

[2] To whom correspondence should be addressed: 1501 San Pablo St., ZNI 111, Los Angeles, CA 90033. Tel.: 323-442-4326; Fax: 323-442-4404; E-mail: tulmer@usc.edu.

[3] The abbreviations used are: TM, transmembrane; AMPS, 2-acrylamido-2-methyl-1-propanesulfonate; DHPC, 1,2-dihexanoyl-*sn*-glycero-3-phosphocholine; POPC, 1-palmitoyl-2-oleoyl-*sn*-glycero-3-phosphocholine; NBP, N-terminal TM border proline; THD, talin head domain; TEV, tobacco etch virus; MFI, mean fluorescence intensity; PDB, Protein Data Bank; r.m.s., root mean square; OI, outside-in; IO, inside-out.
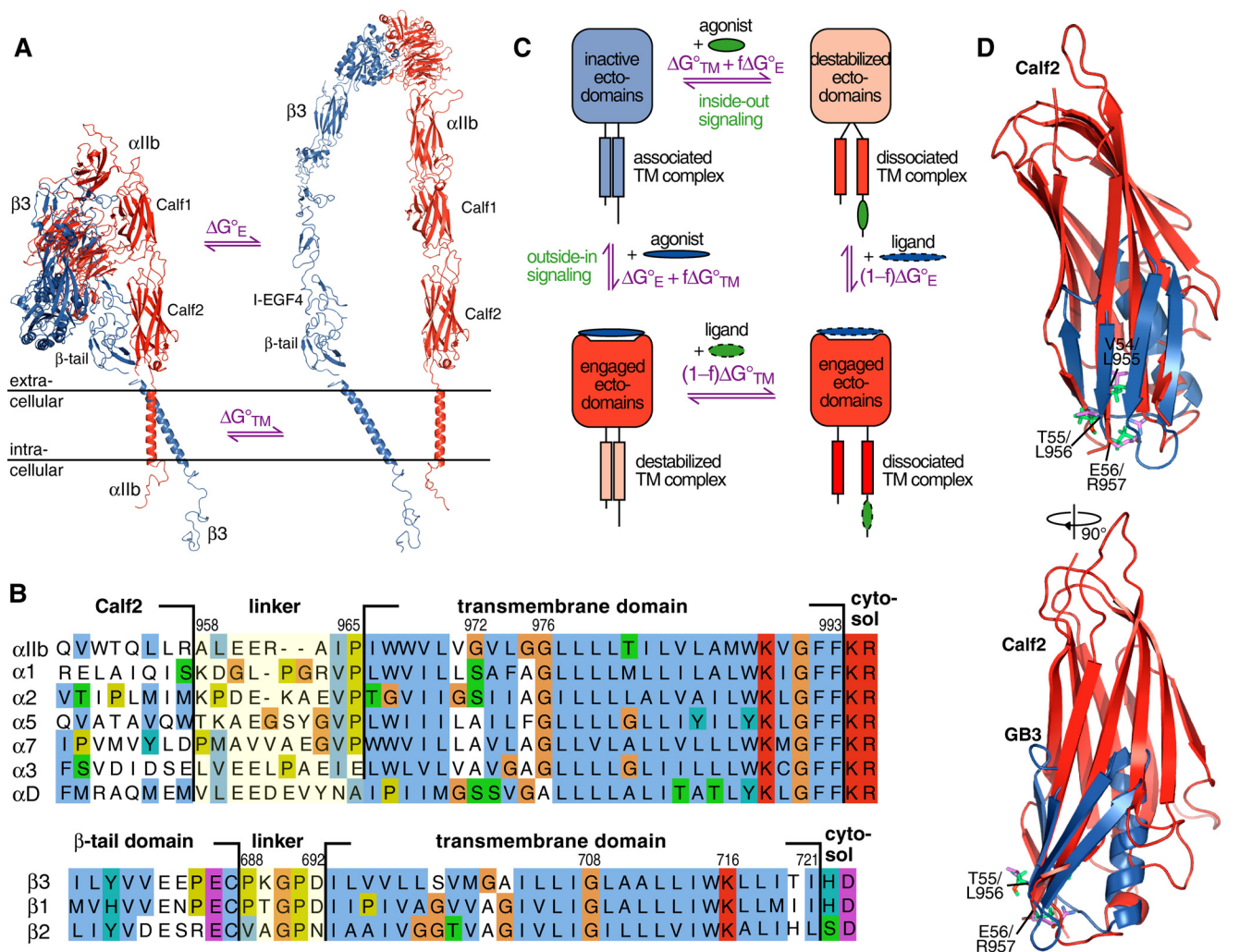
FIGURE 1. **Overview of integrin structure, allosteric integrin regulation, and ecto-TM domain linker sequences.** *A,* structural model of integrin αIIbβ3 in inactive (PDB entries 3fcs and 2k9j) and active conformations (PDB entries 2vdl, 3fcs, 2k1a, and 2rmz). Models follow Ref. 59. *B,* sequence alignment of the ectodomain-linker-TM domain region of selected human integrin α and β subunits. The α ectodomain terminates with the Calf2 domain, whereas the β ectodomain terminates with the β-tail domain. Depicted domain borders are based on integrin αIIbβ3 ecto- and TM domain structures (11, 25, 26). Sequence alignment of all 18 human α subunits are provided in Ref. 12. *C,* on a thermodynamic level, integrin bidirectional signaling entails at least four receptor states. In inside-out signaling, an intracellular agonist with an affinity corresponding to at least $\Delta G^{\circ}_{IO} = \Delta G^{\circ}_{TM} + f \cdot \Delta G^{\circ}_{E}$ breaks the ectodomain-stabilized TM complex. At which point the resting ectodomain is sufficiently destabilized to allow the binding of an extracellular ligand with an affinity corresponding to at least $(1 - f) \cdot \Delta G^{\circ}_{E}$. Outside-in signaling proceeds analogously. For visual clarity, departing agonists and ligands are not shown. *D,* structural alignment of the Calf2 domain of integrin αIIb with the GB3 domain (PDB entries 3fcs and 2oed, respectively). The side chains of the three C-terminal residues are shown in *ball-and-stick* representation. A GB3(T55L) substitution was implemented to match the corresponding side chain of Calf2.

In the present study, we use NMR spectroscopy to characterize the linker structure, dynamics, and ecto-TM domain coupling of integrin αIIb in model constructs, evaluate its sequence determinants in relationship to other integrin α subunits, and assess its effects on receptor activation in cellular integrin activation assays. We further compare the sequence and structural features of the ecto-TM domain coupling of integrin αIIb with other human TM cell surface receptors to achieve general insight into the principles of TM cell surface receptor signaling.

Results and Discussion

Thermodynamic Description of Ectodomain-TM Domain Coupling—To obtain a simple model of integrin activation, we decompose the free energy required to activate the receptor into two terms. Specifically, the threshold of bi-directional TM

signaling relates to the free energy difference between the dissociated and associated TM complex, termed ΔG°_{TM}, and between the inactive and active ectodomain conformations, termed ΔG°_{E} (Fig. 1*A*). However, the physical linkage between the TM and ectodomains must determine their allosteric coupling and ultimately set signaling thresholds. To quantify the mutual stabilization of the TM complex and the ectodomain (12), we define a coupling factor, *f*, with $0 \leq f \leq 1$. To activate the ectodomain via inside-out (IO) signaling, talin binding has to provide $\Delta G^{\circ}_{IO} = \Delta G^{\circ}_{TM} + f \Delta G^{\circ}_{E}$ (Fig. 1*C*). Conversely, to disrupt the TM complex and generate an outside-in (OI) signal, an extracellular agonist must provide $\Delta G^{\circ}_{OI} = f \cdot \Delta G^{\circ}_{TM} + \Delta G^{\circ}_{E}$. Moreover, *f* sets the minimum affinity of an extracellular ligand to bind to an inside-out stimulated receptor, namely $(1-f) \cdot \Delta G^{\circ}_{E}$, and analogously $(1-f) \cdot \Delta G^{\circ}_{TM}$ for an intracellular ligand in an OI-stimulated receptor (Fig. 1*C*).
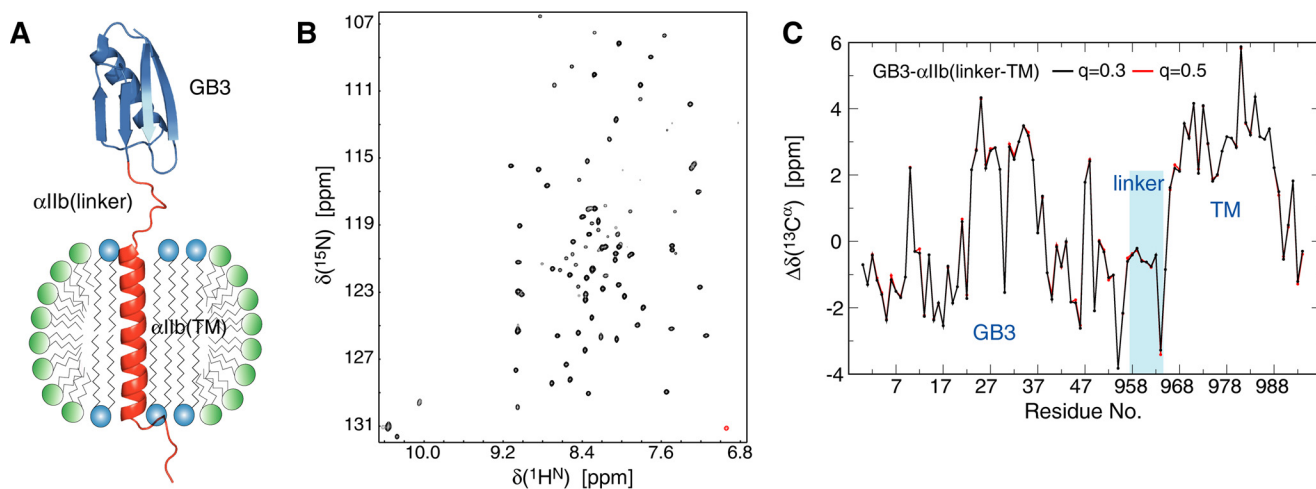
FIGURE 2. **Illustration of GB3-linker-TM construct, NMR spectral quality, and influence of bicelle size on protein secondary structure.** *A,* model of the bicelle-immersed GB3-αIIb(linker-TM) construct. PDB entries 2oed and 2k1a were used. *B,* H^N-N transverse relaxation-optimized spectroscopy-type correlation spectrum of 1 mM $^2H/^{13}C/^{15}N$-labeled GB3-linker-TM protein in 350 mM DHPC, 105 mM POPC, 25 mM HEPES-NaOH (pH 7.4), 6% D_2O, 0.02% NaN_3 solution at 700 MHz and 40 °C. *C,* comparison of secondary $^{13}C^\alpha$ shifts, $\Delta\delta(^{13}C^\alpha)$, of GB3-linker-TM domains as a function of bicelle *q*-factor. Bicelles solutions with $q = 0.5$ and 0.3 contained either 350 mM DHPC, 175 mM POPC or 350 mM POPC, 105 mM POPC, respectively. Random coil $\Delta\delta(^{13}C^\alpha)$ shifts are expected at -0.5 ppm because of H^α deuteration.

For the prevalent integrin β1, β2, and β3 subunits, the ecto-TM domain linker sequence is conserved and consists of only 5 residues (Fig. 1*B*). With integrin α subunits on the other hand, longer linker lengths and higher sequence variability were observed (Fig. 1*B*), suggesting that modulation of *f* in the integrin family takes place through the properties of α subunits. Accordingly, our study focused on integrin α subunits, in particular αIIb that exhibits an 8-residue ecto-TM domain linker (Fig. 1*B*) and combines with β3 to form the integrin αIIbβ3 fibrinogen receptor.

A Flexible Linker Loosely Couples the Ecto- and TM Domains in Integrin αIIb—Crystallographic studies of inactive ectodomains provided precise borders of the membrane-proximal αIIb(Calf2) and β3(β-tail) domains but were unable to obtain structural information on linkers (11, 23, 24). NMR studies of the αIIb and β3 TM domains provided borders for these segments (12, 25, 26), but without the representation of preceding αIIb(Calf2) and β3(β-tail) domains, linker properties are invariably misrepresented. Calf2 has an immunoglobulin-like, β-sandwich-fold with longer and more abundant β-sheets compared with typical Ig-like domains (Fig. 1*D*). The elongated shape of Calf2 means that most of these secondary structures are far from the membrane (Fig. 1*A*) and, thus, cannot influence the linker structure. Likewise, crystal structures of Calf2 verify its folding in the absence of linker (11, 23). It is therefore possible to approximate Calf2 with a smaller, highly stable domain that is structurally homologous to the membrane-proximal structure of Calf2 to facilitate the solution NMR-based characterization of linker properties. The third IgG-binding domain of protein G, termed GB3, ensures a transition from the terminal β-sheet to the first linker residue that is similar to Calf2 (Fig. 1*D*). Next to the close congruence of backbone conformations, side chain conformations matched between Calf2 and GB3 for the final three residues preceding the linker. We note that the terminal GB3 residue Glu[56] is hydrogen bonded to Lys[10], providing it a stable backbone structure despite its C-terminal position (27). Thus, whereas all structural aspects pertaining to

the study of ΔG°_E would require an intact ectodomain, a meaningful characterization of *f* is achievable within a construct that fuses GB3 to the αIIb(linker-TM) sequence (Fig. 2*A*).

The GB3-linker-TM construct was reconstituted in phospholipid bicelles (Fig. 2, *A* and *B*), a well established membrane mimic for integrins (15, 26, 28). To control for any size-dependent effect of the bicelle bilayer area on protein structural properties, bicelles with different short-to-long chain lipid ratios ($q = 0.5$ and 0.3) were examined. Backbone chemical shift assignments were carried out in both environments and the obtained secondary $^{13}C^\alpha$ shifts allowed for the straightforward assessment of secondary structure (29). Identical $^{13}C^\alpha$ shifts in $q = 0.5$ and 0.3 bicelles (Fig. 2*C*) showed the absence of bicelle size-dependent effects, allowing us to proceed with $q = 0.3$ bicelles that afford more sensitive measurements. In further validation of the GB3-linker-TM construct, the GB3 structure remained intact in proximity to the bicelle and the TM structure of αIIb was unchanged by the presence of GB3 (Fig. 3*A*). The 8-residue linker exhibited random coil properties with the notable exception of Ile[964], which was coerced into extended conformations by the side chain constraints of succeeding Pro[965] (30). In the absence of the GB3 domain, the linker exhibited helical propensity (positive secondary $^{13}C^\alpha$ shifts; Fig. 3*A*), confirming the requirement of a Calf2 domain representation.

To gain further insight into linker properties, linker backbone dynamics on the pico- to nanosecond time scale were analyzed relative to the TM domain by interpreting the ^{15}N relaxation parameter in terms of the general order parameter S^2 (31). This parameter describes the spatial fluctuation of the N-H bond vector and is limited by $0 \leq S^2 \leq 1$. In case of $S^2 \rightarrow 1$, relaxation is solely described by the global motion of the protein, whereas for $S^2 \rightarrow 0$ local motions fully describe ^{15}N relaxation. In comparison to the well folded TM region ($S^2 \approx 1$), the elevated linker dynamics confirmed its random-coil nature (Fig. 3*C*). To express the rigidity of the GB3 domain-TM domain coupling with a single parameter, the average linker S^2 value, termed $\langle S^2 \rangle_{linker}$, was used. $\langle S^2 \rangle_{linker}$, not being directly
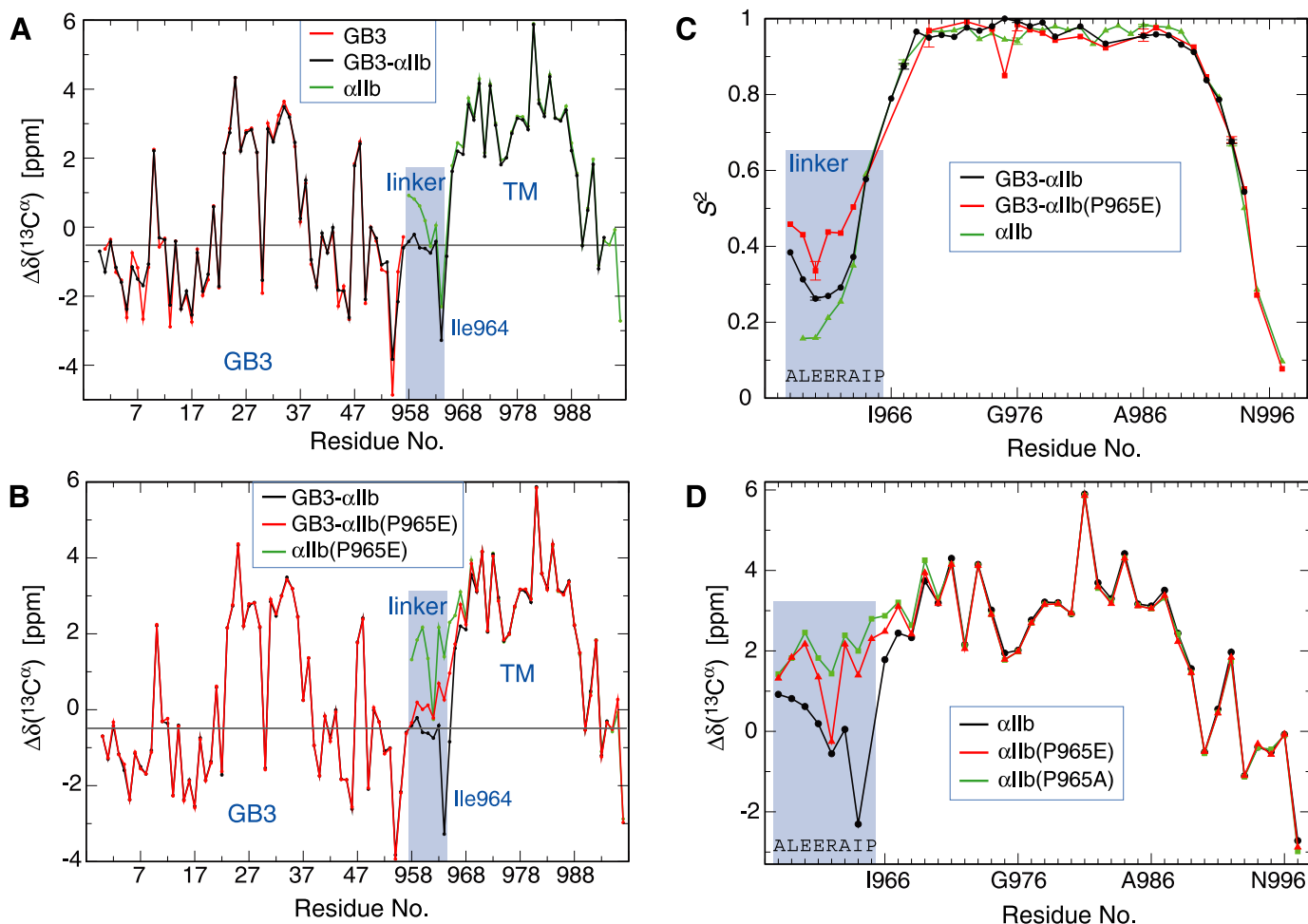
FIGURE 3. **Backbone conformation and dynamics of the ecto-TM domain linker of integrin αIIb.** *A*, comparison of secondary $^{13}C^\alpha$ shifts, $\Delta\delta(^{13}C^\alpha)$, of the GB3 domain, the linker-TM domain, and the GB3-linker-TM domains. Random coil $\Delta\delta(^{13}C^\alpha)$ shifts are expected at -0.5 ppm because of H^α deuteration. *B*, comparison of $\Delta\delta(^{13}C^\alpha)$ of the GB3-linker-TM domains, GB3-linker(P965E)-TM domains, and linker(P965E)-TM domain. *C*, comparison of general order parameter, S^2, for the linker-TM domain and the linker-TM portion of GB3-linker-TM domains and GB3-linker(P965E)-TM constructs. *D*, comparison of secondary $^{13}C^\alpha$ shifts, $\Delta\delta(^{13}C^\alpha)$, of linker-TM domains for αIIb, αIIb(P965E), and αIIb(P965A). Error bars in chemical shift measurements approximate the size of data symbols. For visual clarity, representative S^2 error bars are given for selected residues only.

related to the thermodynamically defined f, was 0.35 ± 0.01. Evidently, a dynamically unstructured linker uncouples the ecto- and TM domain of the integrin αIIb subunit to a substantial degree.

The C-terminal Linker Proline Governs Ecto-TM Domain Coupling—The most conspicuous linker property is the effect of the C-terminal linker proline on its preceding residue (Fig. 3*A*). This proline also represents the most conserved linker residues; 11 of 18 human integrin α subunits contain a proline at their putative TM domain border (Fig. 1*B*). We hypothesized this proline to be a key determinant of the linker-TM transition. To ascertain the role of αIIb(Pro^{965}) on ecto-TM domain linker properties, we have substituted it with Glu, the corresponding residue found in the integrin α3 subunit (Fig. 1*B*), and expanded our NMR study to the GB3-linker(P965E)-TM construct. The glutamate substitution of the linker-terminal proline had profound effects; it led to the propagation of helical propensity from the TM helix into the linker (Fig. 3*B*). The P965E substitution concomitantly diminished backbone dynamics (Fig. 3*C*) and, with $\langle S^2 \rangle_{\text{linker}} = 0.43 \pm 0.02$, enhanced GB3 domain-TM domain coupling, demonstrating $f_{\text{wt}} < f_{\alpha\text{IIb}(\text{P965E})}$. The tighter

TABLE 1
Isotropic rotational correlation times (τ_c) of GB3 and αIIb TM domains

Construct	τ_c(GB3 domain)	τ_c(TM domain)
	ns	*ns*
GB3[a]	3.4 ± 0.1	
Linker-TM[b]		21.0 ± 0.1
GB3-linker-TM[b]	8.2 ± 0.1	24.8 ± 0.1
GB3-linker(P965E)-TM[b]	9.6 ± 0.1	26.2 ± 0.1

[a] In aqueous solution at 24 °C as reported by ref. (27).
[b] In 350 mM DHPC, 105 mM POPC, 25 mM HEPES-NaOH (pH 7.4), solution at 35 °C. The linker-TM value is taken from Ref. 28.

domain-domain coupling was further reflected by an increase in isotropic rotational correlation times of GB3 and TM domains upon substituting Pro^{965} (Table 1).

To examine any effects on $\Delta G°_{\text{TM}}$ as a result of αIIb(P965E), isothermal titration calorimetry was applied to determine the TM complex stability of αIIb(P965E)β3. To broaden our study, we further examined the alanine substitution of αIIb(Pro^{965}), which is found in the integrin αD subunit (Fig. 1*B*). The secondary $^{13}C^\alpha$ shifts of linker(P965A)-TM and linker(P965E)-TM peptides showed an even more helical linker in P965A compared with P965E (Fig. 3*D*). Relative to $\Delta G°_{\text{TM}} = -4.84 \pm 0.01$

TABLE 2

Thermodynamic parameter of αIIbβ3 TM association

In 43 mM DHPC, 17 mM POPC, and 25 mM NaH$_2$PO$_4$/Na$_2$HPO$_4$ (pH 7.4) at 28 °C.

Peptides	$K_{XY}{}^a$	ΔH^o	$T\Delta S^o$	ΔG^o
		kcal/mol	*kcal/mol*	*kcal/mol*
αIIb + $\beta3^a$	3250 ± 60	−16.0 ± 0.1	−11.1 ± 0.1	−4.84 ± 0.01
αIIb(P965A) + β3	2790 ± 50	−12.9 ± 0.1	−8.1 ± 0.1	−4.75 ± 0.01
αIIb(P965E) + β3	2680 ± 50	−16.3 ± 0.1	−11.5 ± 0.1	−4.73 ± 0.01

[a] The wild-type αIIbβ3 value is taken from Ref. 57.

kcal/mol of wild type, TM complex stabilities of αIIb(P965E)β3 and αIIb(P965A)β3 were reduced by 0.11 ± 0.01 and 0.09 ± 0.01 kcal/mol, respectively (Table 2). These small differences indicate that any functional effect of Pro[965] substitutions will be dominated by changes in f and not $\Delta G^\circ{}_{TM}$. In conclusion, by uncoupling the linker from the TM domain conformation, the C-terminal linker proline is a pivotal determinant of linker properties and ecto-TM domain coupling.

The N-terminal TM Border Proline Modulates the Efficiency of Integrin αIIbβ3 Activation—In adopting a membrane-centric view, the C-terminal linker proline is referred to as the N-terminal TM border proline (NBP). To determine the functional significance of the NBP residue and the factor f, we compared the efficiency of talin-induced activation of full-length integrin for αIIbβ3, αIIb(P965A)β3, and αIIb(P965E)β3. Furthermore, we assayed the variant αIIb(E961G/A963G) β3, which resembles the glycine content and distribution of the integrin α5 linker (Fig. 1B). Because of the intrinsic flexibility of glycine, this variant served as negative control, *i.e.* $f_{\alpha\text{IIb(E961G/A963G)}}$ $<$ f_{wt} $<$ $f_{\alpha\text{IIb(P965X)}}$. Talin binds the cytosolic tail of the β3 subunit (19), which dissociates the αIIbβ3 TM complex (32, 33) and destabilizes the resting ectodomain to allow ligand binding (Fig. 4A). An increasing degree of ecto-TM domain coupling (f value) increasingly aligns the dissociated TM complex with the active ectodomain conformation. In the regime where linker mutations do not spontaneously cause receptor activation, we expect increasing values of f to result in higher saturating talin concentrations to compensate for a more favorable, decreased $\Delta G^\circ{}_{IO}$ (Fig. 4A). Concomitantly, with increasing f the threshold for ligand binding is lowered (Fig. 4A) and higher levels of active receptor as judged by successful ligand binding are expected.

We used a cellular assay that correlates the concentration of the talin head domain (THD) with the levels of active integrin αIIbβ3 receptors in the plasma membrane of CHO cells (Fig. 4B). Specifically, a maximal activation index, termed PAC1$_{max}$, was used to quantify the levels of PAC1 ligand-binding competent receptors at saturating THD concentration. The [THD] at which $B_{max}/2$ was reached is termed EC$_{50}$. EC$_{50}$ values carried uncertainties of ~20%; as such, they did not allow the differentiation of linker variants in terms of EC$_{50}$ (Fig. 4C). However, PAC1$_{max}$ values unambiguously increased with increasing values of f as expected. We further note that PAC1$_{max}$ was larger for αIIb(P965A) than αIIb(P965E) that is in line with the higher helical propensity of the linker for αIIb(P965A) than αIIb (P965E), *i.e.* $f_{\alpha\text{IIb(P965E)}}$ $<$ $f_{\alpha\text{IIb(P965A)}}$ (Fig. 3D). Accordingly, we demonstrate in intact receptors (Fig. 1A) that the ecto-TM domain linker properties (f factor) govern the allosteric properties of integrin αIIbβ3 and establish NBP to be a central determinant of such properties.

An N-terminal Proline Frequently Borders the TM Helix of Bitopic Membrane Proteins—The functional relevance and sequence prevalence of NBP in integrin α subunits suggested that it may be a recurring motif in bitopic membrane proteins. Proline is a well established N-terminal helix cap. Its propensity to populate the helix-preceding residue (N$_{cap}$ position) and the first helix residue (N$_1$ position) is documented for membrane proteins (34–36). However, no systematic study regarding the prevalence of NBP in bitopic and polytopic membrane proteins is available. We therefore searched the human genome for proteins with a single-pass TM helix and a preceding sequence of at least 90 residues to allow for the presence of a soluble domain and intervening linker. In defining the NBP motif, we accepted both N$_{cap}$ and N$_1$ positions as both sites serve to abrogate helical propensity in the linker C terminus. NBP residue predictions were found in 20.9% of such proteins (Table 3 and supplemental Table S1). Next to integrin α subunits, NBP is common in receptor-tyrosine kinases, immunological and cytokine receptors (Table 3), revealing a wide relevance of NBP in TM cell surface receptors. For α chains of MHC class I molecules and some killer cell immunoglobulin-like receptors TM sequences were highly homologous (supplemental Table S1). When considering only one representative from these families, the NBP frequency was 17.4%. In contrast, in polytopic membrane proteins in the human genome, the NBP prediction frequency was only 12.4% per TM helix. This difference in frequencies is statistically significant ($p < 0.001$). It appears that bitopic membrane proteins overproportionally benefit from the NBP-conferred sharp separation of linker and TM helix conformations in accordance with an additional functional role of NBP.

The Structure of the Cytokine Receptor Common Subunit β Validates Its NBP Residue—To verify the presence of NBP in another prevalent TM cell surface receptor family, we examined our NBP prediction for Pro[441] of the cytokine receptor common subunit β (βc; Table 3). The βc subunit partakes in the heterodimeric assembly of granulocyte-macrophage colony-stimulating factor, interleukin-3 and interleukin-5 receptors (37). Similar to Calf2 of αIIb, the βc ectodomain concludes with an IgG-like domain and transitions into the putative six-residue ^{436}TESVLP^{441} linker from a terminal β-sheet. To define the role of Pro[441], we have determined the TM domain structure of βc and βc(P441A) including flanking residues in phospholipid bicelles by multidimensional, heteronuclear NMR spectroscopy. Backbone and side chain torsion angle restraints in combination with H-N, C$^\alpha$-C′, and C′-N bond vector restraints defined the backbone heavy atoms to precisions of 0.42 and 0.19 Å for βc and βc(P441A), respectively (Table 4). The TM helix of wild-type βc encompassed Met^{442}-Tyr^{466} (Fig. 5A), *i.e.* 25 resi-
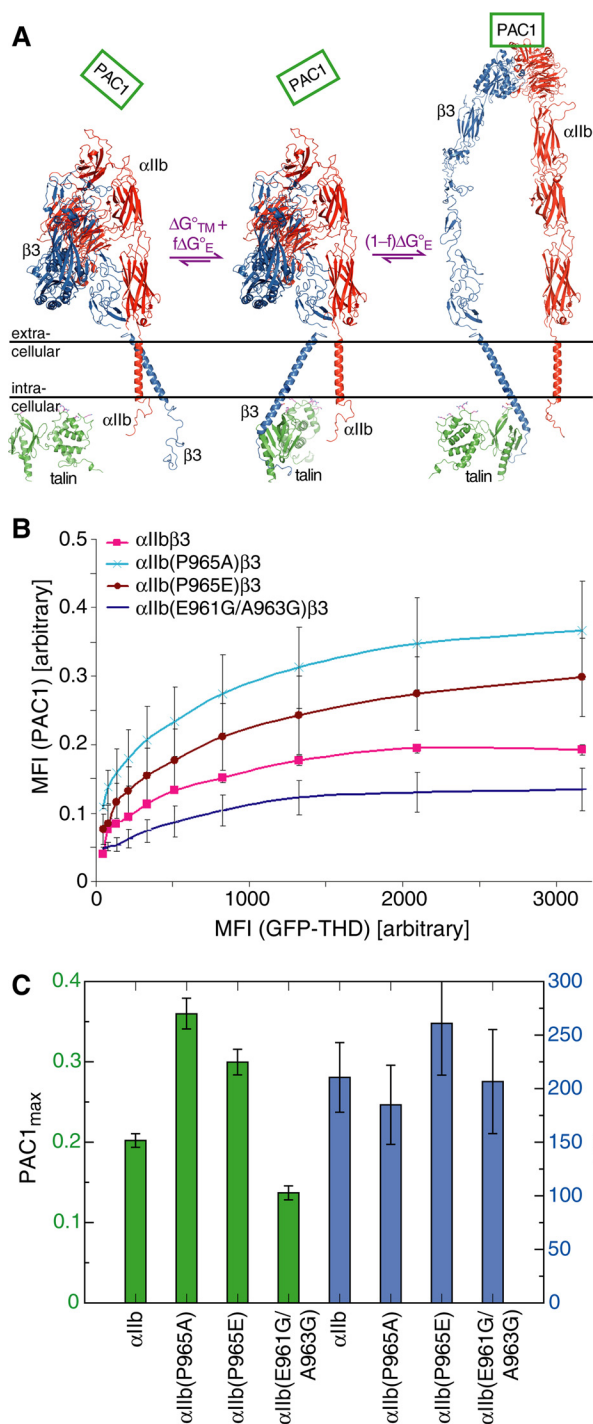
FIGURE 4. Efficiency of talin-mediated integrin αIIbβ3 activation as a function of ecto-TM domain linker sequence. *A,* structural model of cellular assay. GFP-tagged THD breaks the TM complex ($\Delta G°_{IO} = \Delta G°_{TM} + f\Delta G°_E$) at saturating cytosolic concentration as depicted by the binding of talin F3-F2 domains to the β3 tail. The ensuing destabilization of the resting ectodomains allows binding of the ligand-mimetic PAC1 antibody (($1-f)\Delta G°_E$). PDB entries 2vdl, 3fcs, 2k9j, 2k1a, 2rmz, and 3g9w were used. *B,* comparison of receptor activation as a function of linker sequence. Levels of ligand binding-competent receptors were measured as a function of THD concentration. Specifically, the geometric MFI of PAC1 as a function of the MFI of GFP-tagged THD was evaluated. *C,* comparison of levels of integrin activation (PAC1$_{max}$) and talin concentration at PAC1$_{max}$/2 (EC$_{50}$ values). Data are represented as mean ± S.E.

dues, which signifies a small tilt in the membrane. On the C-terminal side, a glycine-Schellmann motif terminates the helix, whereas on the N-terminal side, Pro[441] indeed caps the helix.

The residue preceding Pro[441] was dynamically unstructured at random-coil conformations (Fig. 5*B*), thereby uncoupling linker and TM helix structures.

The structure of βc(P441A) showed a helix extension that folds the entire linker stretch (TESVLA) into helical conformation (Fig. 5*A*), resulting in a relatively long helix of 31 residues (Thr[436]-Tyr[466]) in the absence of the ectodomain. However, lipid interactions remained virtually unchanged between βc and βc(P441A) (Fig. 5*C*). The helix extension is therefore not lipid immersed but remained in the aqueous milieu. Interestingly, the βc(P441A) helix is not fraying at the N terminus but rather starts at Thr[436] without significantly affecting preceding residues (Fig. 5*B*). As a result, without NBP, the ecto- and TM domains of βc would be tightly coupled (Fig. 5*A*).

Conclusions—The linker connecting the ecto- and TM domains of integrin αIIb is flexible. Even in the absence of NBP, the linker must be considered flexible relative to the folded secondary structure (Fig. 3*C*). However, the degree of linker flexibility in integrin α subunits appears to be carefully controlled; 39% of subunits lack NBP, subunits exhibit conspicuous and varying numbers of glycine and proline, and variations in linker lengths (Fig. 1*B*). On structural and functional levels, such variations adjust the degree of ecto-TM domain coupling (Fig. 3*C*) and control receptor activation thresholds (Fig. 4*C*). Correspondingly, flexibility is key to allowing allostery in integrin signaling (Fig. 1*C*) and the same result is expected for other TM cell surface receptors. Our assertion is supported by a 21% incidence of NBP in human single-pass TM proteins, a statistically significant increase of NBP in single over multipass TM helices, and the requirement of NBP to obtain a short, dynamic linker in the cytokine receptor βc subunit (Fig. 5). Accordingly, whereas NBP supports TM helix initiation and TM helix-helix loop formation in general (34–36), the abundance and uncoupling effect of NBP in TM cell surface receptors indicate that the degree of ecto-TM domain coupling plays an important role in the function and signaling mechanism of these proteins.

Experimental Procedures

Integrin αIIb and βc TM Peptide Production and NMR Sample Preparation—GB3-linker-TM constructs of integrin αIIb were derived from the previously introduced pET44-GB3-TEV-linker-TM vector (25). An XhoI site, which codes for Leu-Glu, was introduced into the linker (Fig. 1*B*), and subsequently GB3 with a T55L substitution was subcloned into this vector via this site and a 5′ NdeI site. This procedure eliminated the tobacco etch virus (TEV) protease cleavage site as to express His-tagged GB3(T55L)-αIIb(Ala[958]-Pro[998]). The αIIb(linker-TM) peptides, encompassing αIIb(Ala[958]-Pro[998]), were expressed using the original pET44-GB3-TEV-linker-TM vector with P965A and P965E substitutions. The gene coding for Lys[431]-Lys[473] of human β$_c$ (Uniprot entry IL3RB_HUMAN) was synthesized from overlapping oligonucleotides (38) and cloned into the pET-44 expression vector with GB3 as N-terminal fusion protein and an intervening TEV protease cleavage site. A P441A mutant was created by QuikChange mutagenesis (Stratagene). ^{2}H/^{13}C/^{15}N isotope labeling and protein purifica-

TABLE 3

Examples of human single-pass membrane proteins containing NBP

See supplemental Table S1 for a complete list.

Index	Transmembrane and flanking sequences	Protein
1	SSQPTIPIVGIIAGLVLLGAVITGAVVAAVMWRRKSSDRKGGSYT	HLA class I histocompatibility antigen, A-1 alpha chain
72	TPEPHLPLSLILSVVTSALVAALVLAFSGIMIVYRRKHQELQAMQ	ALK tyrosine kinase receptor
79	QSLSEPILWIVSYALMSVCGAILLVLIVLLLLPFRCQRRPRDPEV	Beta-secretase 2
82	LPRLTPWIVAVAVILMVLGLLTIGSIFFTWRLYNERPRERRNEFS	Butyrophilin subfamily 1 member A1
93	EALIHPTGLSTGALVAILLCIVILLVTVVLFAALRRQRKKEPLII	Cadherin-6
101	TWSTPVQPMALIVLGGVAGLLLFIGLGIFFCVRCRHRRRQAERMS	T-cell surface glycoprotein CD4
119	RSRSLAPVLCGIAAGLILLTFLIVITLYVISKHRARNYYTDTSQK	Complement receptor type 2
120	PDEFLFTPVVVACMSIMALLLLLLLLLLLYKYKQKPKYQVRWKIIE	Macrophage colony-stimulating factor 1 receptor
133	TNGPKIPSIATGMVGALLLLLVVALGIGLFMRRRHIVRKRTLRRL	Epidermal growth factor receptor
142	SELREQLPLIAGSAAAGVVFVVSLVAISIVCSRKRAYSKEAVYSD	Ephrin type-B receptor 1
145	LTPSDLDPLILTLSLILVVILVLLTVLALLSHRRALKQKIWPGIP	Erythropoietin receptor
146	EQRASPLTSIISAVVGILLVVVLGVVFGILIKRRQQKIRKYTMRR	Receptor tyrosine-protein kinase erbB-2
152	LQLPTPVWFHVLFYLAVGIMFLVNTVLWVTIRKELKRKKKWDLEI	High affinity immunoglobulin gamma Fc receptor I
181	QAWPNFLPLVVLVLLLTLAVIAILLFILLWHLCWPKEKADPYPYP	IGF-like family receptor 1
185	TESVLPMWVLALIVIFLTIAVLLALRFCGIYGYRLRRKWEEKIPN	Cytokine receptor common subunit β
194	RALEERAIPIWWVLVGVLGGLLLLTILVLAMWKVGFFKRNRPPLE	Integrin αIIb
212	SETGNPRHLHVLIGTSVVIILFILLLFFLLHRWCCNKKNAVVMDQ	Killer cell immunoglobulin-like receptor 2DL3
262	SDSLLTLPAIVGIGGGGGLLLLVIVAVLIAYKRKSRDADRTLKRL	Plexin-A1
273	FPPSDETPIIAVMVALSSLLVIVFIIIVLYMLRFKKYKQAGSHSN	Receptor-type tyrosine-protein phosphatase alpha
284	AQQSYWPHFVTVTVLFALVLSGALIILVASPLRALRARGKVQGCE	Semaphorin-4A

TABLE 4

Structural statistics for the cytokine receptor βc subunit and its P441A-substituted variant

	βc[a]	βc(P441A)[a]
R.m.s. deviations from experimental dihedral restraints (deg)		
All (βc *70*; βc(P441A) *81*)	0.6 ± 0.2	0.9 ± 0.1
R.m.s. deviations from experimental residual dipolar couplings (Hz)[b]		
$^1D_{NH}$ (βc *20*; βc(P441A) *30*)	1.2 ± 0.2	1.7 ± 0.1
$^1D_{NC'}$ (βc *22*; βc(P441A) *25*)	2.5 ± 0.2	2.1 ± 0.1
$^1D_{C\alpha C'}$ (βc *22*; βc(P441A) *26*)	2.1 ± 0.1	2.0 ± 0.1
R.m.s. deviations from experimental distance restraints (Å)		
All (βc *38*; βc(P441A) *38*)	0.04 ± 0.01	0.04 ± 0.01
Interresidue sequential ($|i - | = 1$) (βc *14*; βc(P441A) *14*)	0.00 ± 0.00	0.00 ± 0.00
Interresidue short range ($1 \langle |i - j| \rangle 5$) (βc *24*; βc(P441A) *24*)	0.05 ± 0.01	0.05 ± 0.01
Deviations from idealized covalent geometry		
Bonds (Å)	0.003 ± 0.000	0.003 ± 0.000
Angles (deg)	0.48 ± 0.02	0.55 ± 0.02
Impropers (deg)	0.37 ± 0.03	0.43 ± 0.03
Coordinate precision (Å)[c]		
Backbone non-hydrogen atoms	0.42	0.19
All non-hydrogen atoms	0.91	0.72
Measures of structural quality		
E_{LJ} (kcal mol^{-1})[3][d]	−154.6	−159.8
Residues in most favorable region of Ramachandran plot[e]	100%	100%

[a] Statistics for all 20 calculated simulated annealing structures, encompassing structured residues M442-G467 for βc and structured residues Thr[436]-Gly[467] for βc(P441A).
[b] R.m.s. deviations are normalized to an alignment tensor magnitude of 10 Hz.
[c] Defined as the average r.m.s. difference between the 20 simulated annealing structures and the mean coordinates.
[d] The Lennard–Jones van der Waals energy was calculated with the CHARMM PARAM 19/20 parameters and not included in the simulated annealing target function.
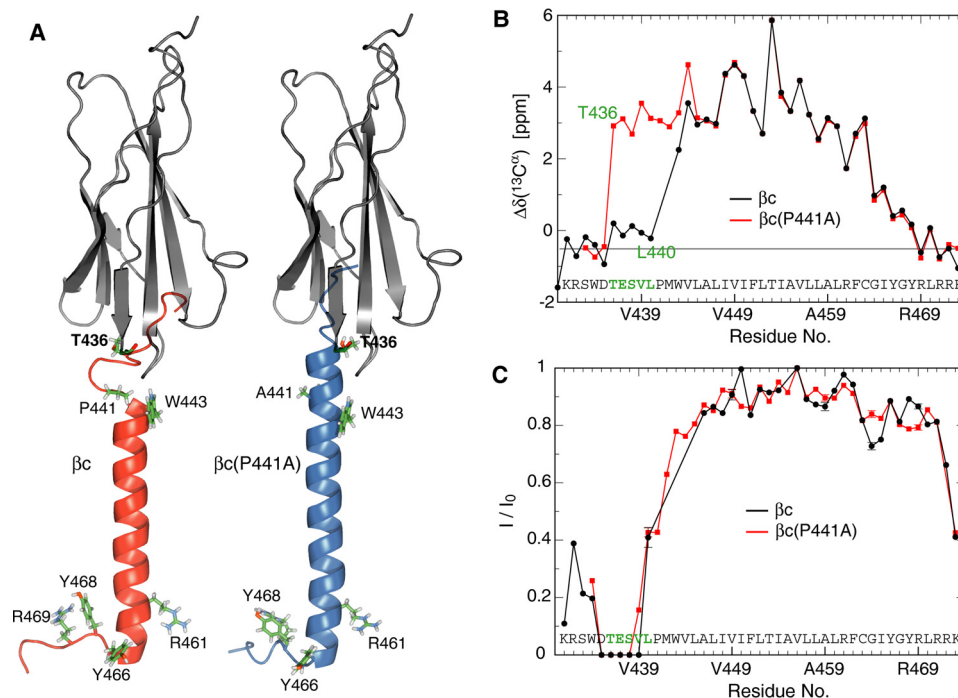[e] Calculated using PROCHECK V3.4.4 (58).

FIGURE 5. **Structure of the TM domain of the cytokine receptor common subunit β (βc) and P441A variant.** *A*, solution structures of bicelle-embedded βc and βc(P441A)-TM domains. For reference, the membrane-proximal domain of the βc ectodomain is shown in *dark gray* (PDB entry 3cxe) (60). *B*, comparison of secondary $^{13}C^{\alpha}$ shifts, $\Delta\delta(^{13}C^{\alpha})$, of βc and βc(P441A) TM domains. Random coil $\Delta\delta(^{13}C^{\alpha})$ shifts are expected at -0.5 ppm because of H$^{\alpha}$ deuteration. *C*, protection of backbone $^{1}H^{N}$ nuclei of βc and βc(P441A) TM domains from paramagnetic Mn^{2+}EDDA^{2-} in the aqueous phase. I/I_0 quantifies the ratio of $^{1}H^{N}$-^{15}N NMR resonances intensities in the presence and absence of 1 mM Mn^{2+}EDDA^{2-}, respectively (26).

tion was carried out as described for wild-type αIIb(linker-TM) peptide (25).

Defined amounts of freeze-dried protein was taken up in a volume of 320 μl of 350 mM 1,2-dihexanoyl-*sn*-glycero-3-phosphocholine (DHPC), 105 mM 1-palmitoyl-2-oleoyl-*sn*-glycero-3-phosphocholine (POPC), and 25 mM HEPES-NaOH (pH 7.4), 6% D$_2$O, 0.02% NaN$_3$ to yield protein concentrations of 0.6 mM αIIb(linker-TM), 1 mM GB3-αIIb(linker-TM), and 0.5 mM β_c(TM) constructs. For β_c constructs, samples contained an additional 10 mM tris(2-carboxyethyl)phosphine. To acquire residual dipolar couplings for β_c and β_c(P441A), the peptide-bicelle complexes were aligned relative to the magnetic field by stretched, negatively charged polyacrylamide gels of 320 μl volume (39). For β_c, the gel was polymerized in a 6-mm cylinder from a 5.0% (w/v) solution of acrylamide, 2-acrylamido-2-methyl-1-propanesulfonate (AMPS) and bisacrylamide, with a monomer to cross-linker ratio of 49:1 (w/w) and a molar ratio of 97:3 of acrylamide to AMPS. For β_c(P441A), a 4.6% (w/v) solution was used with a 95:5 molar ratio of acrylamide to AMPS. ^{2}H splittings of 0.7 and 0.6 Hz were observed for β_c and β_c(P441A), respectively.

NMR Spectroscopy, Calculation of General Order Parameter S^2, and Structure Calculation—NMR data were acquired on a cryoprobe-equipped Bruker Avance 700 spectrometer at 40 °C unless otherwise stated. HNCA, HNCACB, and HNCO experiments were performed to achieve backbone assignments. HNCO-based experiments were employed for the measurement of $^3J_{C'C\gamma}$ and $^3J_{NC\gamma}$ couplings (40), and the detection of $^1J_{C\alpha C'}$ and $^1J_{C'N}$ as well as $^1J_{C\alpha C'}$ + $^1D_{C\alpha C'}$ and $^1J_{C'N}$ + $^1D_{C'N}$ couplings (41, 42). $^1J_{NH}$ and $^1J_{NH}$ + $^1D_{NH}$ couplings were measured using the ARTSY scheme (43). To determine H^N-H^N and

H^N-H^O NOEs, a ^{15}N-edited NOESY spectrum was recorded (150 ms mixing time). Transverse relaxation-optimized spectroscopy-type H-N detection (44) was used throughout all experiments.

In reference to previous measurement conditions (28), ^{15}N longitudinal and transverse relaxation rates R_1 and R_2, respectively, and {^{1}H}-^{15}N NOEs were measured at 35 °C using transverse relaxation-optimized spectroscopy-based pulse sequences (45). Specifically, {^{1}H}-^{15}N NOE measurements were performed in an interleaved manner with 5 s of presaturation preceded by a recycling delay of 4 s for the NOE experiment and by a 9-s recycle delay for the reference experiment. R_2 measurements were carried out with a CPMG delay of 400 μs. Data were processed and analyzed with the NMRPipe package (46). For R_1 and R_2 quantifications, peak intensities were fit to exponential decay and uncertainties estimated by Monte Carlo simulations as described in the literature (47). The error in {^{1}H}-^{15}N NOE values was estimated by assuming that the uncertainty in the peak heights in the two interleaved spectra equals the r.m.s. noise in each spectrum. ^{15}N relaxation parameters were analyzed with the program Tensor2 (48). An isotropic rotational diffusion tensor adequately described the relaxation data, as verified by using tensors of different symmetries to compare experimental and back-calculated relaxation parameter using χ^2 statistics. To appropriately fit the general order parameter S^2 and to determine its uncertainty, Monte Carlo simulations and *F*-statistics were used (48).

The structures of the bicelle-embedded TM segments of β_c and β_c(P441A) were calculated by simulated annealing, starting at 3000 K using the program XPLOR-NIH (49). Backbone dihe-

dral angle constraints were obtained from the pattern of N, H$^\alpha$, C$^\alpha$, C$^\beta$, and C' chemical shifts (50). $^3J_{C'C\gamma \text{ and }}$ $^3J_{NC\gamma}$ coupling constants instructed χ_1 side chain angle restraints. Aside from standard force field terms for covalent geometry (bonds, angles, and improper dihedrals) and nonbonded contacts (Van der Waals repulsion), dihedral angle and interproton distance restraints were implemented using quadratic square-well potentials. In addition, a backbone-backbone hydrogen-bonding potential and torsion angle potential of mean force were employed (51, 52). A quadratic harmonic potential was used to minimize the difference between predicted and experimental H-N, C$^\alpha$-C', and C'-N residual dipolar couplings ($\Delta^1 D$). The final values for the force constants of the different terms in the simulated annealing target function were as previously described (12). Table 4 reports the structural statistics for the total of 20 structures calculated for β_c and β_c(P441A). Ensemble coordinates for β_c and β_c(P441A) together with energy-minimized average structures and structural constraints have been deposited in the Protein Data Bank codes 2na8 and 2na9 and Biological Magnetic Resonance Bank as entries 25931 and 25932.

Talin-dependent Integrin αIIbβ3 Activation—CHO-K1 cells were transfected with 2.5 μg of αIIb cDNA and 2.5 μg of β3 cDNA in conjunction with either 1 μg of GFP talin head domain (GFP-THD) or 0.1 μg of GFP as control. Cells were cultured for 24 h after transfection, trypsinized, washed, and co-stained with anti-αIIbβ3 antibody D57 detecting αIIbβ3 expression in the phycoerythrin channel and with the ligand-mimetic antibody PAC1 (53, 54) reporting αIIbβ3 activation in the Alexa 647 channel. The inability of PAC1 to activate integrin αIIbβ3 is noted (53, 54). Phycoerythrin-positive, *i.e.* αIIbβ3-expressing, cells were gated and further divided into 12 regions according to the expression level of talin head domain in these cells. The geometric mean fluorescence intensity (MFI) of GFP-THD were calculated from each population and plotted against the MFI of PAC1 (Fig. 4B). PAC1$_{max}$ and EC$_{50}$ values were extracted by non-linear curve fitting.

Isothermal Titration Calorimetry—ITC measurements of the peptides listed in Table 2 were carried on a Microcal VP-ITC calorimeter. 10 μM β3 peptide in the 1.425-ml sample cell was titrated with αIIb peptide by injecting 9-μl aliquots over a period of 10 s each. Measurements were carried out in 43 mM DHPC, 17 mM POPC, and 25 mM NaH$_2$PO$_4$/Na$_2$HPO$_4$ (pH 7.4) at 28 °C. Prior to data analysis, the measurements were corrected for the heat of dilutions of the αIIb and β3 peptides. The αIIbβ3-TM complex stoichiometry was fixed at the experimentally verified 1:1 ratio (55) and the reaction enthalpy (ΔH^o) and K_{XY} were calculated from the measured heat changes, δH_i, as described (55).

Human Genome Analysis—Entries from the Uniprot KB database with a location tag of "single pass," organism tag of "*Homo sapiens* (human) (9606)," and "Reviewed" status were selected. To allow for the possibility of linker, domain, and signal sequence to precede the TM helix, only entries with at least 90 residues preceding the annotated TM sequence were considered. 1597 entries fulfilled these criteria. Using the program TMHMM 2.0 (56), the annotated TM sequences were re-evaluated, which left 1557 entries as some TM annotations were discarded. When predicted TM borders were accurate, entries

with Pro at positions -1 (N$_{cap}$) and $+1$ (N$_1$) were sought. However, inspection of the predictions for integrin subunits and other entries suggested a maximal N-terminal TM border accuracy of ± 1 residues. We therefore accepted Pro at positions -2, -1, $+1$, and $+2$ but discarded entries in which a negatively charged residue succeeded proline (*e.g.* integrin β3; Fig. 1B) as this residue is likely to constitute the N$_{cap}$ position. 326 entries fulfilled these criteria (supplemental Table S1). For reference, Pro at positions -1, $+1$ produced 213 entries (13.7%). To compare single to multipass entries, analogous Uniprot entries with location tag "multipass" were selected. Of a total of 15,889 predicted TM helices in these proteins, 1971 exhibited Pro at positions -2, -1, $+1$, and $+2$.

For multipass TM helices, the NBP-containing proportion is $p_1 = y_1/n_1 = 1971/15889 = 0.124$. As to single-pass helices without overrepresented families (see "Results and Discussion"), $p_2 = y_2/n_2 = 259/1490 = 0.174$. To ascertain whether it is true that $p_1 < p_2$, a two-tailed Z-test was performed. The test statistic is $Z = (p_1\text{-}p_2)/(p^*(1\text{-}p^*)(1/n_1 + 1/n_2))^{0.5}$, where $p^* = (y_1 + y_2)/(n_1 + n_2)$. With $Z = -5.49$ the hypothesis was accepted ($p < 0.001$).

References

1. Hynes, R. O. (2002) Integrins: bidirectional, allosteric signaling machines. *Cell* **110,** 673–687
2. Iwamoto, D. V., and Calderwood, D. A. (2015) Regulation of integrin-mediated adhesions. *Curr. Opin. Cell Biol.* **36,** 41–47
3. Winograd-Katz, S. E., Fässler, R., Geiger, B., and Legate, K. R. (2014) The integrin adhesome: from genes and proteins to human disease. *Nat. Rev. Mol. Cell Biol.* **15,** 273–288
4. Schlessinger, J. (2014) Receptor tyrosine kinases: legacy of the first two decades. *Cold Spring Harbor Perspect. Biol.* **6,** pii a008912
5. Kovacs, E., Zorn, J. A., Huang, Y., Barros, T., and Kuriyan, J. (2015) A structural perspective on the regulation of the epidermal growth factor receptor. *Annu. Rev. Biochem.* **84,** 739–764
6. Maruyama, I. N. (2015) Activation of transmembrane cell-surface receptors via a common mechanism? the "rotation model". *Bioessays* **37,** 959–967
7. Scheck, R. A., Lowder, M. A., Appelbaum, J. S., and Schepartz, A. (2012) Bipartite tetracysteine display reveals allosteric control of ligand-specific EGFR activation. *ACS Chem. Biol.* **7,** 1367–1376
8. Bessman, N. J., Freed, D. M., and Lemmon, M. A. (2014) Putting together structures of epidermal growth factor receptors. *Curr. Opin. Struct. Biol.* **29,** 95–101
9. Lu, C., Mi, L. Z., Grey, M. J., Zhu, J., Graef, E., Yokoyama, S., and Springer, T. A. (2010) Structural evidence for loose linkage between ligand binding and kinase activation in the epidermal growth factor receptor. *Mol. Cell Biol.* **30,** 5432–5443
10. Xiong, J. P., Stehle, T., Diefenbach, B., Zhang, R., Dunker, R., Scott, D. L., Joachimiak, A., Goodman, S. L., and Arnaout, M. A. (2001) Crystal structure of the extracellular segment of integrin αVβ3. *Science* **294,** 339–345
11. Zhu, J., Luo, B. H., Xiao, T., Zhang, C., Nishida, N., and Springer, T. A. (2008) Structure of a complete integrin ectodomain in a physiologic resting state and activation and deactivation by applied forces. *Mol. Cell* **32,** 849–861
12. Lau, T.-L., Kim, C., Ginsberg, M. H., and Ulmer, T. S. (2009) The structure of the integrin αIIbβ3 transmembrane complex explains integrin transmembrane signalling. *EMBO J.* **28,** 1351–1361

13. Li, R., Babu, C. R., Valentine, K., Lear, J. D., Wand, A. J., Bennett, J. S., and DeGrado, W. F. (2002) Characterization of the monomeric form of the transmembrane and cytoplasmic domains of the integrin β3 subunit by NMR spectroscopy. *Biochemistry* **41,** 15618–15624

14. Ulmer, T. S., Yaspan, B., Ginsberg, M. H., and Campbell, I. D. (2001) NMR analysis of structure and dynamics of the cytosolic tails of integrin αIIbβ3 in aqueous solution. *Biochemistry* **40,** 7498–7508

15. Surya, W., Li, Y., Millet, O., Diercks, T., and Torres, J. (2013) Transmembrane and juxtamembrane structure of αL integrin in bicelles. *PLoS ONE* **8,** e74281

16. Weljie, A. M., Hwang, P. M., and Vogel, H. J. (2002) Solution structures of the cytoplasmic tail complex from platelet integrin αIIb- and β3-subunits. *Proc. Natl. Acad. Sci. U.S.A.* **99,** 5878–5883

17. Xiong, Y. M., Chen, J., and Zhang, L. (2003) Modulation of CD11b/CD18 adhesive activity by its extracellular, membrane-proximal regions. *J. Immunol.* **171,** 1042–1050

18. Grigoryan, G., Moore, D. T., and DeGrado, W. F. (2011) Transmembrane communication: general principles and lessons from the structure and function of the M2 proton channel, K⁺ channels, and integrin receptors. *Annu. Rev. Biochem.* **80,** 211–237

19. Tadokoro, S., Shattil, S. J., Eto, K., Tai, V., Liddington, R. C., de Pereda, J. M., Ginsberg, M. H., and Calderwood, D. A. (2003) Talin binding to integrin beta tails: a final common step in integrin activation. *Science* **302,** 103–106

20. Kamata, T., Handa, M., Sato, Y., Ikeda, Y., and Aiso, S. (2005) Membrane-proximal α/β stalk interactions differentially regulate integrin activation. *J. Biol. Chem.* **280,** 24775–24783

21. Wang, W., Fu, G., and Luo, B. H. (2010) Dissociation of the α-subunit calf-2 domain and the β-subunit I-EGF4 domain in integrin activation and signaling. *Biochemistry* **49,** 10158–10165

22. Zhu, J., Carman, C. V., Kim, M., Shimaoka, M., Springer, T. A., and Luo, B. H. (2007) Requirement of α and β subunit transmembrane helix separation for integrin outside-in signaling. *Blood* **110,** 2475–2483

23. Xiong, J. P., Mahalingham, B., Alonso, J. L., Borrelli, L. A., Rui, X., Anand, S., Hyman, B. T., Rysiok, T., Müller-Pompalla, D., Goodman, S. L., and Arnaout, M. A. (2009) Crystal structure of the complete integrin αVβ3 ectodomain plus an α/β transmembrane fragment. *J. Cell Biol.* **186,** 589–600

24. Dong, X., Mi, L. Z., Zhu, J., Wang, W., Hu, P., Luo, B. H., and Springer, T. A. (2012) α(v)β(3) Integrin crystal structures and their functional implications. *Biochemistry* **51,** 8814–8828

25. Lau, T.-L., Dua, V., and Ulmer, T. S. (2008) Structure of the integrin αIIb transmembrane segment. *J. Biol. Chem.* **283,** 16162–16168

26. Lau, T.-L., Partridge, A. W., Ginsberg, M. H., and Ulmer, T. S. (2008) Structure of the integrin β3 transmembrane segment in phospholipid bicelles and detergent micelles. *Biochemistry* **47,** 4008–4016

27. Hall, J. B., and Fushman, D. (2003) Characterization of the overall and local dynamics of a protein with intermediate rotational anisotropy: dsifferentiating between conformational exchange and anisotropic diffusion in the B3 domain of protein G. *J. Biomol. NMR* **27,** 261–275

28. Suk, J. E., Situ, A. J., and Ulmer, T. S. (2012) Construction of covalent membrane protein complexes and high-throughput selection of membrane mimics. *J. Am. Chem. Soc.* **134,** 9030–9033

29. Wishart, D. S., and Case, D. A. (2001) Use of chemical shifts in macromolecular structure determination. in *Nuclear Magnetic Resonance of Biological Macromolecules, Part A* (James, T. L., and Schmitz, V. D., eds) pp. 3–34, Academic Press, Waltham, MA

30. Schimmel, P. R., and Flory, P. J. (1968) Conformational energies and configurational statistics of copolypeptides containing L-proline. *J. Mol. Biol.* **34,** 105–120

31. Lipari, G., and Szabo, A. (1982) Model-free approach to the interpretation of nuclear magnetic resonance relaxation in macromolecules: 1. theory and range of validity. *J. Am. Chem. Soc.* **104,** 4546–4559

32. Kim, C., Lau, T.-L., Ulmer, T. S., and Ginsberg, M. H. (2009) Interactions of platelet integrin αIIb and β3 transmembrane domains in mammalian cell membranes and their role in integrin activation. *Blood* **113,** 4747–4753

33. Kalli, A. C., Wegener, K. L., Goult, B. T., Anthis, N. J., Campbell, I. D., and Sansom, M. S. (2010) The structure of the talin/integrin complex at a lipid bilayer: an NMR and MD simulation study. *Structure* **18,** 1280–1288

34. Ulmschneider, M. B., and Sansom, M. S. (2001) Amino acid distributions in integral membrane protein structures. *Biochim. Biophys. Acta* **1512,** 1–14

35. Landolt-Marticorena, C., Williams, K. A., Deber, C. M., and Reithmeier, R. A. (1993) Nonrandom distribution of amino-acids in the transmembrane segments of human type-I single span membrane-proteins. *J. Mol. Biol.* **229,** 602–608

36. Shelar, A., and Bansal, M. (2014) Sequence and conformational preferences at termini of α-helices in membrane proteins: role of the helix environment. *Proteins* **82,** 3420–3436

37. Hercus, T. R., Dhagat, U., Kan, W. L., Broughton, S. E., Nero, T. L., Perugini, M., Sandow, J. J., D'Andrea, R. J., Ekert, P. G., Hughes, T., Parker, M. W., and Lopez, A. F. (2013) Signalling by the βc family of cytokines. *Cytokine Growth Factor Rev.* **24,** 189–201

38. Hoover, D. M., and Lubkowski, J. (2002) DNAWorks: an automated method for designing oligonucleotides for PCR-based gene synthesis. *Nucleic Acids Res.* **30,** e43

39. Ulmer, T. S., Ramirez, B. E., Delaglio, F., and Bax, A. (2003) Evaluation of backbone proton positions and dynamics in a small protein by liquid crystal NMR spectroscopy. *J. Am. Chem. Soc.* **125,** 9179–9191

40. Hu, J. S., Grzesiek, S., and Bax, A. (1997) Two-dimensional NMR methods for determining (χ1) angles of aromatic residues in proteins from three-bond J(C'Cγ) and J(NCγ) couplings. *J. Am. Chem. Soc.* **119,** 1803–1804

41. Jaroniec, C. P., Ulmer, T. S., and Bax, A. (2004) Quantitative J correlation methods for the accurate measurement of ¹³C'-¹³C[agr] dipolar couplings in proteins. *J. Biomol. NMR* **30,** 181–194

42. Chou, J. J., Delaglio, F., and Bax, A. (2000) Measurement of one-bond N-15-C-13' dipolar couplings in medium sized proteins. *J. Biomol. NMR* **18,** 101–105

43. Fitzkee, N. C., and Bax, A. (2010) Facile measurement of H-1-N-15 residual dipolar couplings in larger perdeuterated proteins. *J. Biomol. NMR* **48,** 65–70

44. Pervushin, K., Riek, R., Wider, G., and Wüthrich, K. (1997) Attenuated T-2 relaxation by mutual cancellation of dipole-dipole coupling and chemical shift anisotropy indicates an avenue to NMR structures of very large biological macromolecules in solution. *Proc. Natl. Acad. Sci. U.S.A.* **94,** 12366–12371

45. Zhu, G., Xia, Y., Nicholson, L. K., and Sze, K. H. (2000) Protein dynamics measurements by TROSY-based NMR experiments. *J. Magn. Reson.* **143,** 423–426

46. Delaglio, F., Grzesiek, S., Vuister, G. W., Zhu, G., Pfeifer, J., and Bax, A. (1995) Nmrpipe: a multidimensional spectral processing system based on Unix pipes. *J. Biomol. NMR* **6,** 277–293

47. Kamath, U., and Shriver, J. W. (1989) Characterization of thermotropic state changes in myosin subfragment-1 and heavy-meromyosin by UV difference spectroscopy. *J. Biol. Chem.* **264,** 5586–5592

48. Dosset, P., Hus, J. C., Blackledge, M., and Marion, D. (2000) Efficient analysis of macromolecular rotational diffusion from heteronuclear relaxation data. *J. Biomol. NMR* **16,** 23–28

49. Schwieters, C. D., Kuszewski, J. J., Tjandra, N., and Clore, G. M. (2003) The Xplor-NIH NMR molecular structure determination package. *J. Magn. Reson.* **160,** 65–73

50. Shen, Y., Delaglio, F., Cornilescu, G., and Bax, A. (2009) TALOS plus: a hybrid method for predicting protein backbone torsion angles from NMR chemical shifts. *J. Biomol. NMR* **44,** 213–223

51. Grishaev, A., and Bax, A. (2004) An empirical backbone-backbone hydrogen-bonding potential in proteins and its applications to NMR structure refinement and validation. *J. Am. Chem. Soc.* **126,** 7281–7292

52. Kuszewski, J., Gronenborn, A. M., and Clore, G. M. (1997) Improvements and extensions in the conformational database potential for the refinement of NMR and x-ray structures of proteins and nucleic acids. *J. Magn. Reson.* **125,** 171–177

53. Shattil, S. J., Cunningham, M., and Hoxie, J. A. (1987) Detection of activated platelets in whole blood using activation-dependent monoclonal antibodies and flow cytometry. *Blood* **70,** 307–315

54. Shattil, S. J., Hoxie, J. A., Cunningham, M., and Brass, L. F. (1985) Changes in the platelet membrane glycoprotein IIb·IIIa complex during platelet activation. *J. Biol. Chem.* **260,** 11107–11114

55. Situ, A. J., Schmidt, T., Mazumder, P., and Ulmer, T. S. (2014) Character-

ization of membrane protein interactions by isothermal titration calorimetry. *J. Mol. Biol.* **426,** 3670–3680

56. Krogh, A., Larsson, B., von Heijne, G., and Sonnhammer, E. L. (2001) Predicting transmembrane protein topology with a hidden Markov model: application to complete genomes. *J. Mol. Biol.* **305,** 567–580

57. Schmidt, T., Suk, J. E., Ye, F., Situ, A. J., Mazumder, P., Ginsberg, M. H., and Ulmer, T. S. (2015) Annular anionic lipids stabilize the integrin αIIbβ3 transmembrane complex. *J. Biol. Chem.* **290,** 8283–8293

58. Laskowski, R. A., Rullmann, J. A., MacArthur, M. W., Kaptein, R., and Thornton, J. M. (1996) AQUA and PROCHECK-NMR: programs for checking the quality of protein structures solved by NMR. *J. Biomol. NMR* **8,** 477–486

59. Dai, A., Ye, F., Taylor, D. W., Hu, G., Ginsberg, M. H., and Taylor, K. A. (2015) The structure of a full-length membrane-embedded integrin bound to a physiological ligand. *J. Biol. Chem.* **290,** 27168–27175

60. Hansen, G., Hercus, T. R., McClure, B. J., Stomski, F. C., Dottore, M., Powell, J., Ramshaw, H., Woodcock, J. M., Xu, Y., Guthridge, M., McKinstry, W. J., Lopez, A. F., and Parker, M. W. (2008) The structure of the GM-CSF receptor complex reveals a distinct mode of cytokine receptor activation. *Cell* **134,** 496–507